



Theoretical analysis for self-sharpening penetration of tungsten high-entropy alloy into steel target with elevated impact velocities

Haihua Chen¹ · Xianfeng Zhang¹ · Chuang Liu¹ · Wei Xiong¹ · Mengting Tan¹ · Lan-Hong Dai^{2,3}

Received: 31 January 2021 / Revised: 15 February 2021 / Accepted: 25 February 2021 / Published online: 16 June 2021
 © The Chinese Society of Theoretical and Applied Mechanics and Springer-Verlag GmbH Germany, part of Springer Nature 2021

Abstract

The “self-sharpening” effect has been observed experimentally in the penetration of tungsten high-entropy alloy (WHEA) into steel targets in previous study. From the microscopic observation of the residual WHEA long-rod projectile (LRP), the multiphase structure at micro-scale of WHEA is the key effects on self-sharpening penetration process. In order to describe the distinctive penetration behavior, the interaction between micro phases is introduced to modify the hydrodynamic penetration model. The yield strengths of WHEA phases are determined based on the solid solution strengthening methods. Combined with the elbow-streamline model, the self-sharpening mechanism is revealed in view of the multi-phase flow dynamics and the flow field in the deformation area of the LRP nose is characterized to depict the shear layer evolution and the shape of the LRP’s nose as well as the determination of the penetration channel. The self-sharpening coefficient considering the reduction of nose radius is proposed and introduced into the penetration model to calculate the depth of penetration and the penetration channel. Results show that the multi-phase interaction at the microscopic level contributes to the inhomogeneous distribution of the WHEA phases. The shear layer evolution separates part of the LRP material from the nose and makes the nose radius decrease more quickly. It is also the reason that WHEA LRPs have a pointed nose compared with the mushroom nose of WHA heavy alloy (WHA) LRPs. The calculated results agree well with the corresponding experimental data of WHA and WHEA LRPs penetrating into semi-infinite medium carbon steel targets with elevated impact velocities.

Keywords Impact dynamics · Long-rod projectile · Tungsten high-entropy alloy (WHEA) · Self-sharpening penetration · Solid solution strengthening

Abbreviations

v	Instantaneous impact velocity
v_0	Initial impact velocity
v_s	Impact velocity when the LRP stops penetration
u	Penetration velocity

Executive Editor: Chao Zhang.

✉ Xianfeng Zhang
 lynx@njust.edu.cn
 Lan-Hong Dai
 lhdai@lnm.imech.ac.cn

¹ School of Mechanical Engineering, Nanjing University of Science & Technology, Xiaolingwei 200, Nanjing 210094, China

² State Key Laboratory of Nonlinear Mechanics, Institute of Mechanics, Chinese Academy of Sciences, Beijing 100190, China

³ School of Engineering Science, University of Chinese Academy of Sciences, Beijing 101408, China

μ'	Poisson’s ratio
ρ_p	LRP density
ρ_t	Target density
l_0	Length of the initial LRP
r_0	Radius of the initial LRP
R_t	Resistance stress
Y_p	Dynamic yield strength of the LRP
ψ	The nose radius after separation to the nose radius before separation
ψ^2	Nose self-sharpening coefficient
r_a	Nose radius after separation
r_b	Nose radius before separation
d	Diameter of LRP rigid portion
D	Diameter of the LRP nose
A_p	Cross-section of LRP undeformed portion
A_d	Cross-section of LRP deformed portion
ω	Ejection velocity at the throw location
K_p	Bulk modulus of LRP
q_p	Stagnation pressure

θ	Angle of material particle in the LRP nose
r_c	Radius of material particle in the LRP nose
p_c	Normal stress on the micro-body
$\sigma_{0,2}^{mix}$	Yield stress from rule of mixture
$\sigma_{0,2}^{cal}$	Calculated yield stress
$\Delta\sigma$	Stress caused by solid solution strengthening
$\Delta\sigma_i$	Stress of solid solution strengthening caused by the i th element
$G_{i,j}$	Shear modulus of i th or j th element
$c_{i,j}$	Concentration of the i th or j th element
f_i	Mismatch parameter
$\delta G_{i,j}$	Atomic modules
$\delta r_{i,j}$	Atomic size mismatch
$r_{i,j}$	Atom radius of i th or j th element
v_c	Tangential velocity of material particle
$p_{dynamic}$	Dynamic stress of LRP nose material
Y_{WHEA}	Yield stress of the WHEA
Y_{FCC}	Yield stress of the WHEA FCC phase
Y_{BCC}	Yield stress of the WHEA BCC phase
Y_{WHA}	Yield stress of WHA
$r_{channel}$	Radius of penetration channel

1 Introduction

Long-rod projectiles (LRPs) with deep penetration capacity have been widely used in the weapon industry recently, such as the armor-piercing projectile and earth-penetrating weapon [1,2]. In past decades, extensive efforts have been made to understand and characterized LRPs penetration behavior [3–14]. Massive new materials with “self-sharpening” property have been developed for high penetration ability of LRPs [15–24]. Among them, our newly developed tungsten high-entropy alloy (WHEA) exhibited a striking “self-sharpening” behavior, which thus leads to 10–20% increase in penetration depth in comparison with conventional WHA at given imposed kinetic energy [18].

The shear sensitivity of the material was thought as the key to reveal the self-sharpening mechanism. The self-sharpening effect of depleted uranium (DU) alloy rods was firstly observed in the penetration experiments due to the adiabatic shear sensitivity [19]. Bulk metallic glass (BMG) easily produces highly localized shear bands [25] and is possible to be chosen as the new material of LRP instead of DU alloy. In order to introduce the self-sharpening phenomenon to the high velocity penetration, W-fiber and W-particle reinforced BMG [16–18,20,21] were employed. The BMG with second phase performed the self-sharpening effect because the BMG with high strength is brittle in most cases and the second phase increases its ductility. However, the occurrence of the self-sharpening effect in the penetration process also required other conditions such as the threshold of impact velocity. Chen et al. [22] and Li et al. [23,24] found the

projectile could not penetrate the target effectively until the impact velocity exceeded a threshold by analyzing the penetration behavior of tungsten fiber reinforced metallic glass composite LRPs. These efforts which have been invested in the penetration self-sharpening behavior promote the process of new penetration mechanisms. In addition, it is also important to describe the new penetration phenomenon based on the analytical models.

Since it is difficult to record transient characteristics of the penetration process in experiments, developing theoretical models to characterize the self-sharpening penetration behavior is necessary. The well-known Alekseevskii–Tate (A–T) model [3,12,13] is a one-dimensional modified Bernoulli equation which has been widely used in related researches. It assumed that the materials near the interface of the target and projectile behaved as fluid while the rear of the projectile remains rigid. Rosenberg et al. [8] improved the A–T model by introducing the equivalent cross-sectional area due to the non-uniformity of the force acting on the mushroom nose from the center to the edge of LRPs. The influence factors including the nose shape [10], the length to diameter ratio [4,9] and the dynamic resistance stress [4,11] of penetration were also investigated. Based on the simulation results of the pressure and velocity field in the penetration process, Walker et al. [7] clarified the relationship between target resistance and penetration velocity by using the cylindrical cavity expansion theory (CET). Lu et al. [14] divided the penetration process into three modes according to different states of penetrators which was controlled by the resultant target resistance force and the dynamic strength of the penetrator. Anderson et al. [6] made a series of elegant works on penetration model and considerable examples were provided of model predictions against experimental data. More efforts [26–29] have further promoted the penetration theory.

In general, additional experimental details were incorporated for development of a more accurate penetration model. In spite of extensive progress, it is noted that theoretical study on the self-sharpening penetration behavior is limited. With more new materials with self-sharpening effects are used in LRPs, penetration mechanisms and analytical models with self-sharpening penetration has been a topic of interests in impact dynamics.

In this paper, to characterize our newly found self-sharpening penetration behavior of WHEA, the properties of each phase were analyzed to explicate the material flow of the LRPs in the penetration process. The flow field characteristics of deformation area in the nose of LRPs were obtained for further analysis of the shear layer evolution. Combined with the microscopic observation, the detailed microstructure studies were conducted to reveal the self-sharpening mechanism in the penetration process. The self-sharpening coefficient was introduced to the penetration model in consideration of the nose radius reduction. In addition, the prediction of

the nose shape variation, the penetration channel formation and the depth of penetration (DOP) were validated by the relevant experimental data. In Sect. 2, the microstructure of WHA and WHEA were observed and the disordered distribution of soft and hard phases is the primary factor associated with self-sharpening effect of WHEA LRP noses. In Sect. 3, based on the microstructure of WHEA LRPs, the multi-phase flow based on fluid dynamics was established using solid dynamics solutions for obtaining yield strength values to describe the self-sharpening penetration effect. The shear layer evolved in the nose caused the separation of the WHEA LRP material. For this case, the shear layer evolution led to the decreased nose radius during the penetration process, and a self-sharpening coefficient was introduced to the classical A–T model. In Sect. 4, the multi-phase interaction at the microscopic level of WHEA LRPs sharpened the nose, and influenced the penetration channel radius, and the DOP. The experiment results of penetration channel radii and the DOP were given and in good accordance with the theoretical results.

2 Microscopic characters of recovered LRPs of WHA and WHEA

The self-sharpening effect of WHEA LRPs was observed in the previous study [18]. In order to reveal the self-sharpening behavior, the WHA LRP was selected to compare with the WHEA and the microstructure was investigated. Based on the microstructure observation, the deformation mechanism at micro-scale was presented.

2.1 Micro-structures of recovered residual LRPs of WHEA and WHA

The original microstructure of the WHEA shows that W distributes in BCC dendrites most, while Fe and Ni are rich in the other two phases. Mo has a relatively homogeneous distribution among the sample. The four components (27.5W–24.4Fe–23.5Ni–24.6Mo, wt%) have different proportion in each phase which caused the diverse mechanical properties of the WHEA phases. The face centered cubic (FCC) phases and the body centered cubic (BCC) phases are the main component phases of the WHEA and the Rhombohedral (μ) phase is the third phase with complicated crystal structure and tiny proportion. The FCC phase is the matrix which wraps the BCC phase and the μ phase. The Vickers hardness of the FCC phase, BCC phase and μ phase is 5.4 GPa, 11.1 GPa and 16.5 GPa, respectively and the elastic modulus of the three phases is 234 GPa, 370 GPa and 313 GPa [18] and the BCC phase takes up 60% and the FCC phase is 40% from the SEM image. The μ phase scattered in the

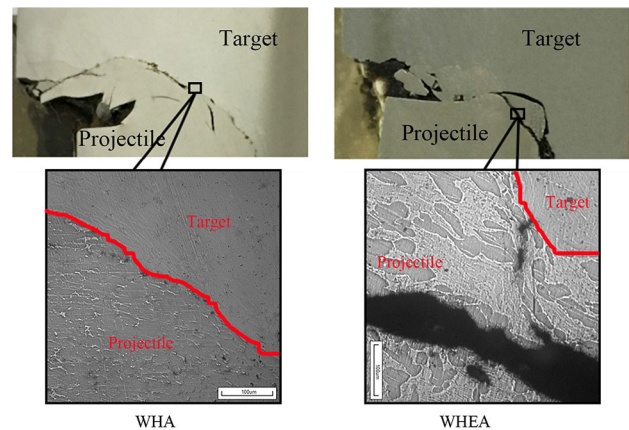


Fig. 1 Comparison between WHA and WHEA LRP penetration

BCC phase and FCC phase, which cannot be distinguished from the SEM image.

The nose shape and microstructure of the residual WHA and WHEA LRP are shown in Fig. 1. It is obviously that the WHA LRP forms a mushroom nose while the WHEA is a pointed one. From the metallographic diagrams of the residual LRP nose edge by optical microscopy, the phases are subjected to severe deformation in the WHEA. The WHA contains 93% W and can be regarded as a uniform material.

2.2 Analysis on deformation mechanism of WHEA LRPs at micro-scale

As discussed in Ref. [12], the LRP and target will behave as fluid if the stress is larger than the dynamic yield strength of both the LRP and target. The material of the LRP and the target behaves as fluid so as to simplify the analysis. The nose of WHA LRP can be regarded as a continuous single-phase fluid. However, the WHEA is a multiphase alloy and hard to be considered as single-phase fluid. In addition, the basic mechanical property of each phase varies considerably. Three phases have apparent difference in Vickers hardness and elastic modulus, which makes it impossible to deal with the WHEA as a homogeneous alloy. How does the WHEA behave during the penetration process? The way to deal with the multi-phase alloy needs to be investigated.

In Li's research [30] of a dual-phase HEA (50Fe–30Mn–10Co–10Cr, wt%), the plastic strain is accommodated primarily by the softer and less confined FCC γ matrix at early stages of deformation. Additional mechanical twinning, dislocation slip and formation of stacking faults in hexagonal close-packed (HCP) ϵ phase are also activated as important deformation mechanisms at later stages of deformation. The WHEA has the similar microstructure with the soft and hard phases and undergoes the same microscopic deforma-

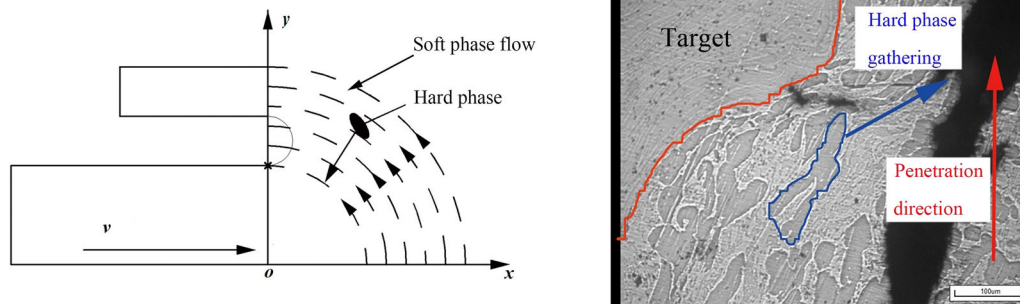


Fig. 2 Movement of the hard phase in the flow field

tion process at high strain rates. When the alloy suffers high pressure, the FCC phase which is the matrix of the alloy starts to deform firstly, while the BCC phase keeps its initial state. In other words, the soft phase forms a flow field and the hard phase is regarded as the particle which flows in the flow field.

The nose of the LRP forms a flow field and the material of LRP continues to flow out in the penetration process [31]. It is also noted that the pressure at the interface between the projectile and the target decreases from the center of the long rod nose to the edge of the crater [8]. The pressure inside of nose is smaller than outside. Accordingly, hard phases flow to the inside of the nose during the pressure gradient caused by the flow field of soft phase. The FCC phase flows out from the nose more easily than the BCC phase and there are more FCC phases in the nose edge near the target in Fig. 2. The hard phases accumulate somewhere inside the nose of the LRP and the relative flow of the two phases causes the formation of cracks. The flow characteristics in the WHEA LRP nose are similar with the particle motion in the turbulence. The particles move from low-velocity regions to high-velocity regions and forms a shear layer. It is also proposed that the pressure in high-velocity regions is lower than that in low-velocity regions [32].

This disordered distribution of the soft and hard phase is the key effect for its self-sharpening penetration. The ratio of the hard phase in the top of the nose, the edge of the nose, the middle part and the tail of the WHEA residual projectile is 76%, 70%, 61% and 57% respectively. It is obvious that the ratio of the hard phase increased in the nose of the residual projectile. The ratio is almost equal in the middle part and the tail of the residual projectile compared with the original WHEA which is 60%. The variation of the distribution of the soft and hard phase gives rise to a more inhomogeneous deformation and cause relatively higher strain gradients, which leads to the shear band formation. Compared with the WHEA, it is difficult for the WHA with continuous and uniform flow field to develop cracks in the LRP nose due to its single-phase structure.

3 Theoretical analysis on self-sharpening penetration of WHEA LRPs

In view of the microstructure of WHEA, it is important to describe the multi-phase flow based on the fluid dynamics. Combined with the theory of solid solution strengthening, the yield strength of the BCC phase and the FCC phase is obtained and the self-sharpening penetration mode of the LRP is related to the microscopic phases. The flow field of WHEA LRP nose is established and the shear layer evolves through the nose which causes the separation of the LRP material. The nose radius of the WHEA LRP decreases in the penetration process. Considering the shear layer evolution and the radius reduction, a self-sharpening coefficient is introduced to the classic A–T model [3,12,13] to describe the WHEA penetration process.

3.1 Solid solution strengthening for the yield strength of WHEA

The strength of WHEA is primarily determined by the mechanical properties of the continuous FCC phase. The FCC phases bear the external pressure from the target and the BCC phases flow in the FCC phases relatively. The local strength of the LRP nose in the penetration progress changes due to the flow of the hard phase. Thus, it is necessary to obtain the dynamic yield strength of the BCC phases and FCC phases.

The large differences in atomic size and shear modulus among solute and solvent will lead to a more obvious solid solution strengthening (SSS). The classical Labusch approach [33,34] has been successfully applied to WHEAs for yield strength prediction and the calculated yield stress of the alloy [35,36] can be described as:

$$\sigma_{0.2}^{cal} = \sigma_{0.2}^{mix} + \Delta\sigma, \quad (1)$$

Table 1 Physical properties of the used gases

Metal	W	Mo	Fe	Ni
r_{atom}	1.41	1.4	1.27	1.25
G (GPa)	131	123	80.3	76
c_i	27.5	24.6	24.4	23.5
$\sigma_{0.2}$	750	438	98	59
δ_{ri}	0.062	0.054	-0.055	-0.073
δ_{Gi}	0.29	0.221	0.25	-0.31
f_i	0.578	0.488	0.507	0.661
$\Delta\sigma_i$ (MPa)	844	627	654	909

where the $\sigma_{0.2}^{mix}$ is the stress by the rule of mixture and the $\Delta\sigma$ is given by SSS. The equation for $\Delta\sigma$ is obtained:

$$\Delta\sigma = \left(\sum \Delta\sigma_i^{3/2} \right)^{2/3}. \quad (2)$$

The SSS caused by the i -th element is expressed as:

$$\Delta\sigma_i = A' G f_i^{4/3} c_i^{2/3}, \quad (3)$$

where A' is a dimensionless material-dependent constant, of which the value is 0.015 [31,32], G is the shear modulus, c_i is the concentration of the i th element and f_i is the mismatch parameter. The parameters can be determined by:

$$\begin{cases} f_i = \sqrt{\delta G_i^2 + \alpha \delta_{ri}^2}, \\ \delta_{ri} = \frac{9}{8} \sum c_j \delta_{rij}, \\ \delta_{Gi} = \frac{9}{8} \sum c_j \delta_{Gij}, \\ \delta_{rij} = 2 \frac{r_i - r_j}{r_i + r_j}, \\ \delta_{Gij} = 2 \frac{G_i - G_j}{G_i + G_j}, \end{cases} \quad (4)$$

where δG_i is the atomic modules and δ_{ri} is the atomic size mismatch. α is 2–4 for screw dislocations and $\alpha \geq 16$ for edge dislocations. In BCC lattice, the value of α is 8. The c_j is the atomic fraction of j th element in the alloy. δ_{rij} is the atomic size difference of elements i and j . δ_{Gij} is the atomic modules difference of elements i and j .

Basis on the microscopic analysis, WHEA contains three phases, namely BCC phase, FCC phase and μ phase [18]. To simplify analysis, the μ phase is regarded as the BCC phase. The lattice parameters for WHEA are given in Table 1.

The $\Delta\sigma$ can be calculated by Eq. (2) and the shear module of the alloy is estimated using the rule of mixture to be 104 GPa. The $\sigma_{0.2}^{cal}$ can be obtained by Eq. (1) as 1073 MPa, which agrees well with the experiment result of 1010 MPa [18].

Table 2 Parameters of FCC phase

Metal	W	Mo	Fe	Ni
c_i	2.4	12.5	40.6	44.5
δ_{ri}	0.109	0.1	-0.009	-0.026
δ_{Gi}	0.494	0.427	-0.044	-0.106
f_i	1	0.913	0.082	0.236
$\Delta\sigma_i$ (MPa)	106	283	25	108

Table 3 Parameters of BCC phase

Metal	W	Mo	Fe	Ni
c_i	57.4	36.6	4	2
δ_{ri}	0.01	0.002	-0.107	-0.121
δ_{Gi}	0.494	0.427	-0.044	-0.106
f_i	0.501	0.427	0.859	0.975
$\Delta\sigma_i$ (MPa)	515	309	179	134

The yield strengths of FCC phase and BCC phase in WHEA can also be calculated in the same way, which is shown in Tables 2 and 3, respectively. The $\sigma_{0.2}^{cal}$ of FCC phase and BCC phase is 508 MPa and 1359 MPa. The dynamic yield stress of BCC and FCC phase can be calculated by $\sigma_{0.2}^{cal}(1 - \mu')/(1 - 2\mu')$, which is 2.3 GPa and 0.86 GPa. μ' is the Poisson's ratio and is 0.3. Similarly, the dynamic yield stress of WHEA is 1.7 GPa.

The dynamic stress at each point changes with the reduction of velocity and the shear layer appears when dynamic stress of the point is less than the threshold of the dynamic stress. The dynamic yield stress of the FCC phase, BCC phase and WHEA are defined as Y_{FCC} , Y_{BCC} , and Y_{WHEA} , respectively. Y_{FCC} is used to set up the flow field and Y_{BCC} is viewed as the dynamic stress threshold of the WHEA. Similarly, Y_{WHA} is set aside for the flow field as well as the dynamic yield stress of WHA due to its single dominant phase.

3.2 Flow field characteristics of WHEA LRP nose based on the elbow-streamline model

The elbow-streamline model was used to describe the distribution of material flow in the WHA LRP nose [37]. However, the assumption of the $D = 2d$ is lack of consideration in the facts that the radius of the penetration channel changes in the penetration process. The nose diameter can be solved by the conservation of momentum equation in impact direction for the control volume as [31]:

$$(1 + \eta)\rho_p \frac{d^2}{4} v^2 + Y_p \frac{d^2}{4} = \int_0^{D/2} 2R P_{\text{axis}} dR, \quad (5)$$

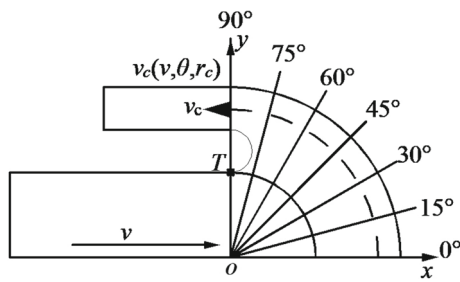


Fig. 3 v_c distribution of the LRP nose at any instantaneous impact velocity

where $\eta = \sin \theta_f$, θ_f is the flow angle of the LRP material. The flow angle is 90°, η equals to 1 in the case. P_{axis} is the pressure on the axis of symmetry of the LRP and is obtained as [38,39]:

$$P_{axis} = q_p \left(1 + \frac{1}{2\xi} + 3\zeta - 1.6\zeta^2 \right), \quad (6)$$

where $\xi = K_p/q_p$, $\zeta = Y_p/q_p$, and $q_p = \rho_p v^2/2$ is the stagnation pressure of an ideal fluid of density ρ_p and velocity v .

The flow field distribution of u - w at a corresponding angle can be calculated and the velocity distribution of the LRP nose during the whole penetration process is obtained. It is assumed that $v_c = v_c(v, \theta, r_c)$, where v_c is the velocity along the tangential direction at the reference point of the nose during the whole penetration process; v is the instantaneous impact velocity of the LRP, θ is the angle at the reference point and r_c is the radius at the reference point. The parameters θ and r_c indicate the position of the reference point in the LRP nose and the parameter v represents the penetration stage. The three-parameter function $v_c = v_c(v, \theta, r_c)$ is used to characterize the flow field model of the LRP nose material during the whole penetration process.

The kinetic energy of the material moving along the tangent direction causes the change of the dynamic pressure in the LRP nose:

$$p_n = \frac{1}{2} \rho_p v_c^2, \quad (7)$$

where p_n is the dynamic pressure of the LRP nose.

The direction of the penetration velocity is defined as 0°, which is regarded as the starting direction and is rotated to 90° in the counterclockwise direction. Reference lines are set every 15°, and the representative model of the v_c value distribution in the nose under any instantaneous impact velocity is established as shown in Fig. 3.

Many factors, such as initial impact velocity, LRP strengths, have influence on the flow field characteristics, among which the initial impact velocity is one of the dominant factors. The nose of WHEA LRP at the instantaneous impact velocity of

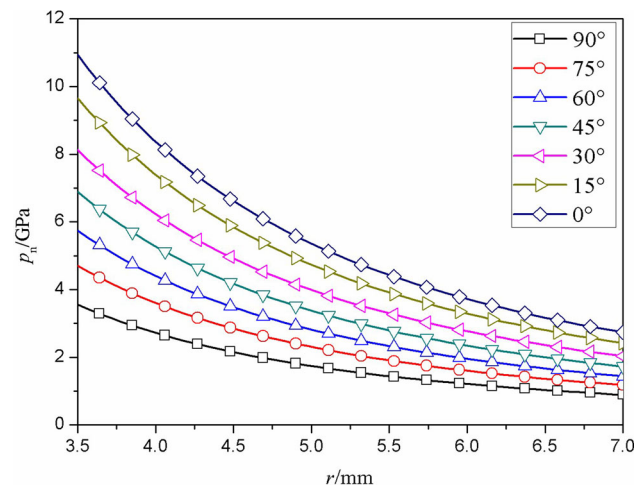


Fig. 4 Distribution of p_n when $v = 1400$ m/s

1400 m/s is taken as an example and the parameters are listed in Table 4. The average kinetic energy is equal to $0.5\rho_p v_c^2$ and the p_n is used to describe the stress distribution in the LRP nose.

The distribution of p_n shows an increasing trend from outside to inside of the nose in Fig. 4. In other words, the p_n increases with the r decreasing at the same angle. Specially, the dynamic pressure on the lower angle is larger than that on the high angle, which shares the common law in the pressure at the interface between the LRP and the target decreases from the center of the long rod nose to the edge of the crater [8].

3.3 Evolution shear layer during penetration of WHEA LRPs

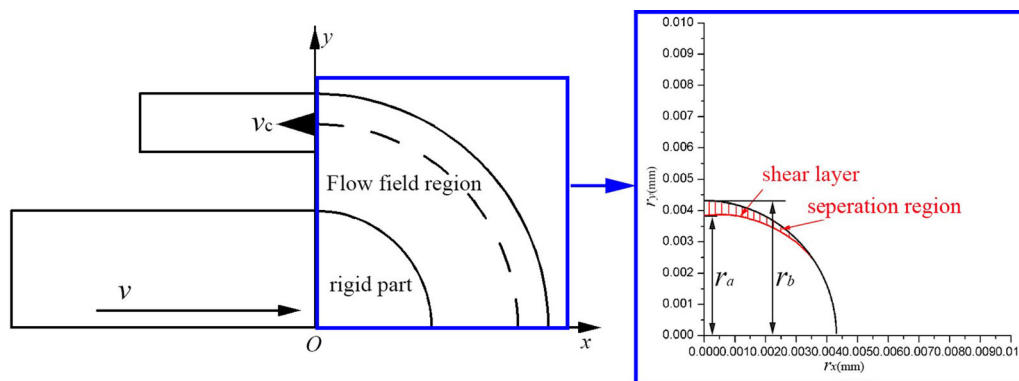
As described in Sect. 2.2, BCC phases flow to the inside of the nose relative to the FCC phase, which causes the disturbance in the flow field. The shear layer develops in the LRP nose and the position of the shear layer is considered as the boundary between the separation region and the flow field region and the similar phenomenon of the shear layer was also validated by [32].

The analytical area is framed by blue lines in Fig. 5. The shear layer develops and the separation part takes shape in the LRP nose. The separation parts split from the nose and the nose radius decreases more sharply during the penetration process. The nose radius before separation is set as r_b and after separation is r_a . The shear layer evolution begins when the flow stress is larger than the dynamic stress threshold and ends when the LRPs stop penetration. The impact velocity when the LRP stops penetration v_s can be solved by [3,12,13]

$$v_s = \sqrt{\frac{2(R_t - Y_p)}{\rho_p}}. \quad (8)$$

Table 4 Parameters of calculation

Parameters	Unit	Value	Description
ρ_p (WHA)	kg/m ³	17500	Density of WHA
ρ_p (WHEA)	kg/m ³	12700	Density of WHEA
ρ_t	kg/m ³	7800	Density of steel target
R_t	GPa	3.4	Target resistance
Y_{WHA}	GPa	1.5	Dynamic yield strength of WHA LRP
Y_{FCC}	GPa	0.86	Dynamic yield strength of FCC phase of WHEA
Y_{BCC}	GPa	2.3	Dynamic yield strength of BCC phase of WHEA
Y_{WHEA}	GPa	1.7	Dynamic yield strength of of WHEA
l_0	m	0.05	Length of the initial LRP
r_0	m	0.0035	Radius of the initial LRP
K_p (WHA)	GPa	285	Bulk modulus of WHA
K_p (WHEA)	GPa	271	Bulk modulus of WHEA

**Fig. 5** Analytical area in the nose of LRPs

In order to illustrate the evolution of shear layer, five impact velocities of 500 m/s, 700 m/s, 900 m/s, 1100 m/s and 1300 m/s are taken as examples. It is obvious that the shear layers are marked at the edge of the LRP nose (Fig. 6). The shear layer and the separation region grows in the flow field with the instantaneous impact velocity decreasing from 1300 to 700 m/s. The outline of the nose is shrunk and the nose become pointed compared with the WHA LRP. Based on the evolution of shear layers and outlines of the LRP nose, the radii of the projectile nose with different impact velocities are obtained, as shown in Fig. 7. It is clear that the nose radius of the WHEA LRP is smaller than that of WHA LRP in the penetration process and more rapid reduction occurs when the shear layer starts to develop. The calculation process of penetration channel is shown in Fig. 7.

3.4 Self-sharpening penetration model based on the shear layer evolution

Further research [40–42] has been done on the long-rod penetration based on A–T model. The diameter ratio of rod nose

and shank η and the nose shape factor N^* were taken into account in the penetration model in [40]. In other words, the maximum radius of the nose (R), the radius of the rod shank (r) and the radius of curvature of the nose shape (S) are the three influence factors which affect the nose shape and the penetration efficiency. Comparing with the model in [40], the ratio of the nose radius after separation (r_a) to the nose radius before separation (r_b) is ψ and the nose self-sharpening coefficient ψ^2 takes the effect of the nose cross-sectional area into consideration. The shear layer evolution in the projectile nose makes the part of the material separate from the nose. The reflection of the self-sharpening effect is the reduction of the projectile nose radius. Here, the ψ^2 is introduced into the A–T model in Eq. (9). The cross-sectional effect was also applied to the penetration in the previous research [8]. The way to determine the value of ψ is the key to the self-penetration model. First, the instantaneous impact velocity decays from v_0 to v_s in the penetration and the radius of penetration channel of corresponding each velocity v_i can be calculated from the Sect. 3.3. Then, the ψ_i of each velocity v_i can be obtained and the mean value of ψ_i is set as the ψ in

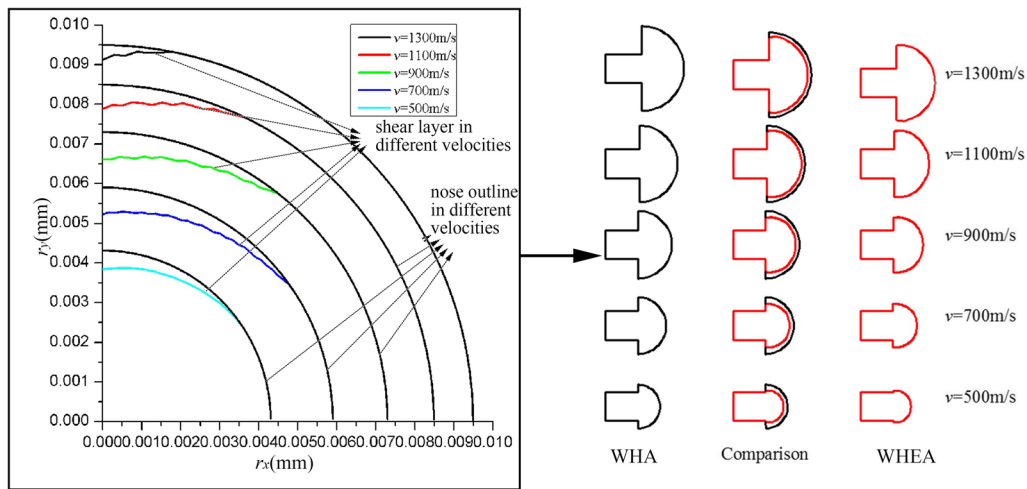


Fig. 6 Shear layer and nose shape of different impact velocities

the penetration whose instantaneous impact velocity decays from v_0 to v_s . The calculation process of ψ is shown in Fig. 8. The multi-phase structure leads to the inhomogeneity in the WHEA projectile. The Y_{bcc} was the threshold of the dynamic stress. The shear layer occurred when the stress in the flow field exceeds the dynamic stress. The radius of the projectile nose and penetration channel decrease and it leads to the separation of the efficient penetration part and invalid penetration part. The ψ was introduced in to the model for the radius decrease.

In general, the radius reduction of the WHEA LRP nose changes the penetration velocity u according to the $v-u$ relation in the following equation

$$Y_p + \frac{1}{2}\rho_p(v-u)^2 = \psi^2 \left(R_t + \frac{1}{2}\rho_t u^2 \right). \quad (9)$$

The relation of $l-v$ is solved by taking the $v = v(u)$ into

$$\int_{l_0}^l \frac{1}{l} dl = \frac{\rho_p}{Y_p} \int (v-u) dv, \quad (10)$$

and the DOP can be solved by the A-T model [3,12,13] in the following equation

$$P = - \int_{v_s}^v \frac{\rho_p}{Y_p} l u dv. \quad (11)$$

4 Results and discussions

As discussed above, the multi-phase interaction in the penetration process sharpens the nose of the WHEA LRP. The

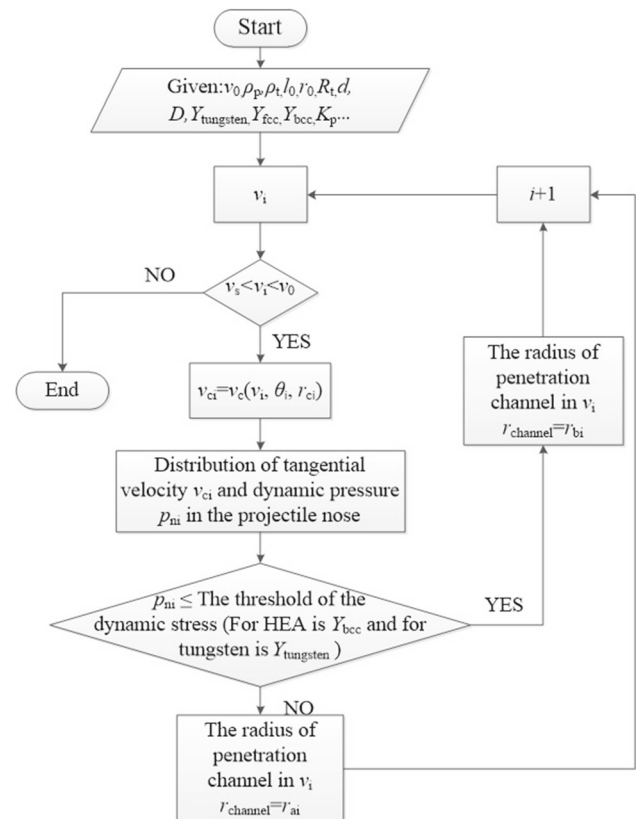


Fig. 7 Calculation process of penetration channel

self-sharpening effect has influence on the penetration channel radius and DOP ultimately. Based on the transformation of the LRP nose shape, the penetration model considering self-sharpening effect is developed to describe the penetration behavior.

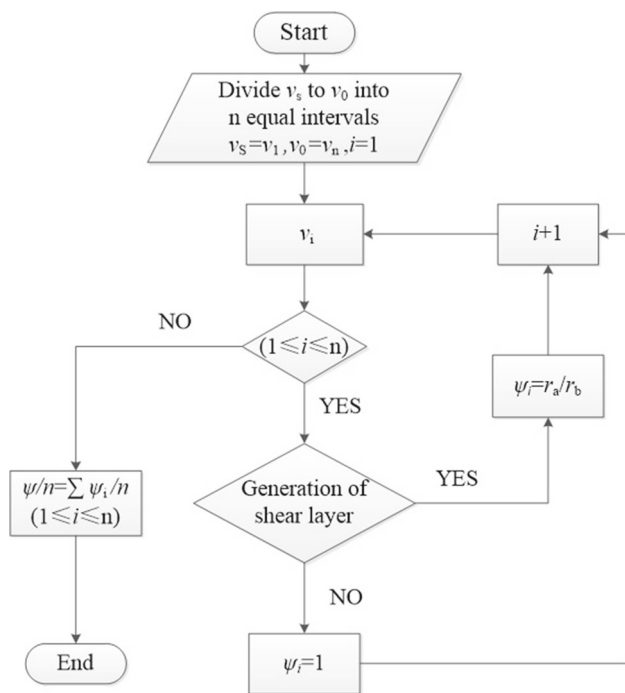


Fig. 8 Calculation process of ψ

4.1 Self-sharpening penetration effects with elevated impact velocities

Based on the evolution of shear layer, the shapes of the LRP nose with different impact velocities are obtained, as shown in Fig. 9. The radii of the WHEA LRP are smaller than that of the WHA at elevated impact velocities. The shear layer occurs when the instantaneous impact velocity reaches 1400 m/s and the downward trend of the WHEA curve is faster than before. Moreover, the nose sharpens more sharply than WHA LRP nose when the shear layer develops in the WHEA LRP. The self-sharpening effect acts on the whole penetration process where the nose radius shrinks at every moment. At the end of the penetration process, the nose shape of the WHEA LRP is pointed compared with the WHA mushroom nose [18] in Fig. 9.

Figure 10 shows the comparison of DOPs versus penetration channel between theoretical results and the test data for the penetration of steel targets by WHA LRPs at different velocities. Taking the interface where LRPs come into contact with targets as the initial position to describe the evolution of penetration channel, the experiment data will exist the negative value when the experimental DOP is larger than the theoretical DOP. The WHA is regarded as a single-phase alloy due to the large proportion of the tungsten phase and the separation region does not occur in the WHA LRP nose. Flow characteristics of WHA are relatively simple. The contents of the two phases are relatively close and phases show more complex mobility behavior. The deformation of the pene-

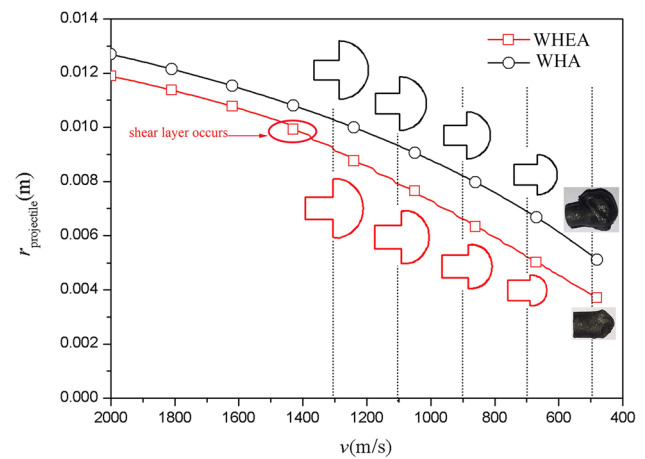


Fig. 9 Comparison between WHA and WHEA LRP nose evolution in penetration process

tration channel degenerates which can be described by the model in [31] mentioned in Sect. 3.1. The calculated result is a continuous smooth curve as the instantaneous impact velocity decreases (Fig. 9). It is seen from Fig. 10 that the predictions by the present model are in good agreement with the experimental data for the impact velocities ranging from 917 m/s to 1181 m/s.

The radius of the WHEA penetration channel decreases faster than that of the WHA when the shear layers start to evolve, which is obviously observed in Fig. 9. The phenomenon is also the reflection of the self-sharpening behavior. Figure 11 shows the penetration channel of the WHEA. The theoretical prediction of the penetration channel evolution shares the same trend with the experimental data. When the LRP impacts the target at lower velocity, the theoretical channel radius near the target surface is smaller than that of the experiment result. The LRP nose occurs brittle fracture at the moment when the LRP hits the target and there is an expansion of the interface between the LRP and the target. It indicates that the WHEA LRP is hard to penetrate into the steel target effectively at low initial impact velocity. The radius of penetration channel in the target interface decreases with the instantaneous impact velocity increasing and the theoretical prediction of the penetration channel evolution is more accurate at higher initial impact velocity ($v_0 = 1330$ m/s).

4.2 Comparison with corresponding experimental results

The relation between DOP and kinetic energy per volume $(\rho v^2)/2$ of WHA and the WHEA are illustrated in Fig. 12. The shear layers do not develop in the WHA LRP nose and the self-sharpening penetration model degenerates into classical A-T model [3,12,13] for the DOP calculation. The shear lay-

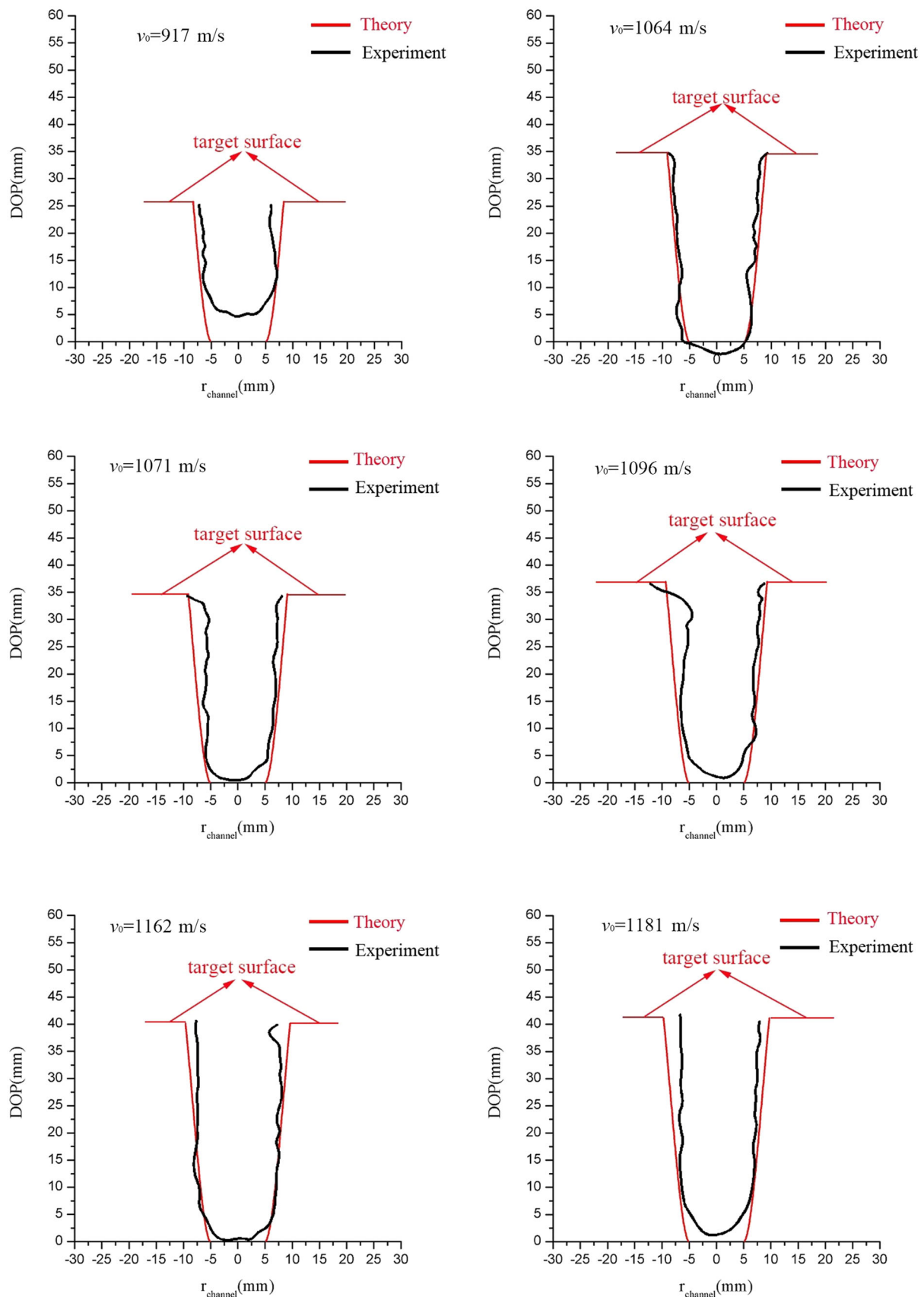


Fig. 10 Comparison between theoretical penetration channel and experimental data of WHA LRP

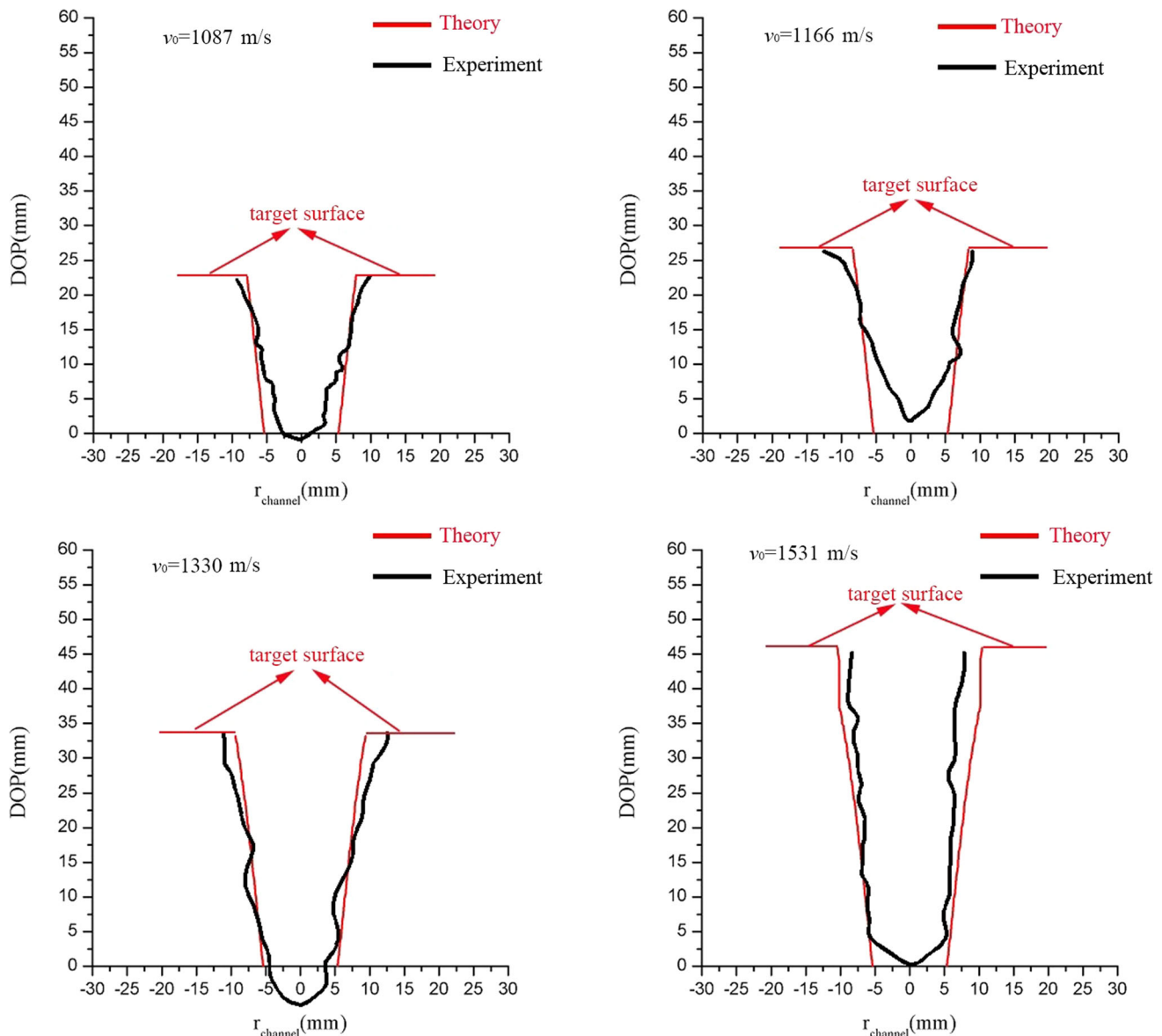


Fig. 11 Comparison between theoretical penetration channel and experimental data of WHEA LRPs

erevolution and the corresponding decrease of the LRP nose radius are considered in the WHEA DOP calculation by Eq. (10). The theoretical results agree well with the experimental data from 5 to 8 kJ/cm³ and the theoretical prediction is smaller than the experimental data when the kinetic energy exceeds 10 kJ/cm³. The ψ is the key factor to the DOP of the WHEA. The value of the ψ is divided into three parts: $\psi > 1$, $\psi = 1$ and $0 < \psi < 1$. It is no physical significance when the $\psi > 1$. The model goes back to A–T model when the $\psi = 1$. The difference between the r_a and r_b increase when the ψ decrease in the range of $0 < \psi < 1$. The relation of u - v changed as well as the flow field of the nose. The DOP increases with the ψ decreasing in the range of 0 to 1.

The difference between the penetration behavior of the WHA and the WHEA should be explained, especially the self-sharpening behavior. It is feasible to take the WHA as single dominant phase alloy. The WHA LRP at high-speed penetration state is subjected to the huge force from the target to generate the recirculation. At this time, the flow of the material at the projectile nose can be regarded as a continuous fluid. The nose of the WHA LRP follows the basic deformation behavior and the evolution of the crack in the single-phase flow field is difficult. According to the analysis on the micro-scale failure mode of the WHEA with two phases, the continuous FCC phase forms the flow field and the hard phase moves towards the inner side of the nose and the shear layer occurs when the pressure exceeds the dynamic

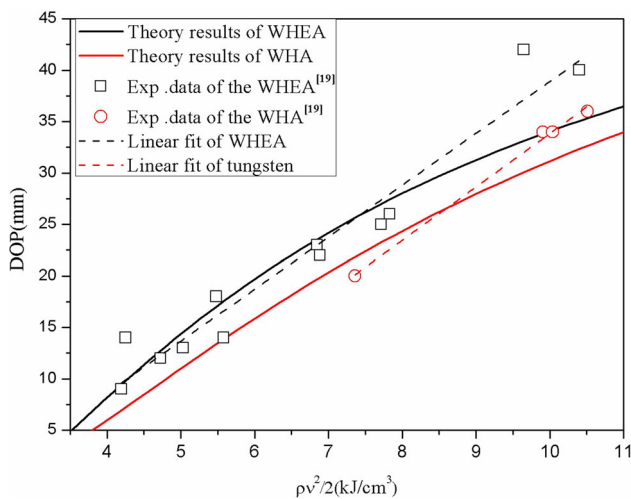


Fig. 12 Comparison between theoretical DOP and the test data

stress threshold. The self-sharpening penetration behavior of the WHEA attributes to the material inhomogeneity and the interaction of the two phases under the special stress state in the LRP nose.

Most of the existing penetration theories are one-dimensional penetration theories, and less attention is paid to the process parameters of penetration. To study the penetration self-sharpening phenomenon, the penetration theory must be developed to two-dimensional and three-dimensional theory. The existing research is not enough to reveal the mechanism of self-sharpening penetration of these kinds of alloys, and the universality of this theoretical model for other materials with similar microstructure needs to be further studied. The future work will focus on the mechanism of self-sharpening and the applicability of the model to other similar materials.

5 Conclusions

In this paper, a theoretical study is presented to depict the self-sharpening effect in the LRP nose. The flow field in the LRP nose is established based on the material inhomogeneity. The solid solution strengthening method which is used to predict the yield strength of the BCC phase, FCC phase and the WHEA for further description of the multi-phase flow. The DOP and radii of penetration channel are obtained by the theoretical model. The main conclusions are as follows:

1. The flow field in the LRP nose during the penetration process is established. The pressure gradient in the LRP nose is also obtained and the multi-phase interaction is the basis of the self-sharpening behavior.
2. The solid solution strengthening is used to calculate the yield strengths of WHEA phases. The flow field of the

LRP nose is structured based on the FCC phase and the Y_{BCC} is set as the dynamic stress threshold to describe the shear layer evolution. The analyzing method can also be applied to the other multi-phase alloy.

3. The self-sharpening penetration model is developed and the nose self-sharpening coefficient ψ^2 is decided based on the nose radius evolution. The theoretical DOP and the penetration channel of the WHEA LRPs are well consistent with the experimental results.

Acknowledgements This work was supported by the National Natural Science Foundation of China (Grant 11790292) and the NSAF Joint Fund (Grant U1730101).

References

1. Di Benedetto, G., Matteis, P., Scavino, G.: Impact behavior and ballistic efficiency of armor-piercing projectiles with tool steel cores. *Int. J. Impact Eng.* **115**, 10–18 (2018)
2. Young, C.W.: Depth prediction for earth-penetrating projectiles. *J. Soil Mech. Found. Div.* **95**(3), 803–817 (1969)
3. Alekseevskii, V.P.: Penetration of a rod into a target at high velocity. *Combust. Explos. Shock Waves* **2**(2), 63–66 (1966)
4. Anderson, C.E., Walker, J.D., Hauver, G.E.: Target resistance for long-rod penetration into semi-infinite targets. *Nucl. Eng. Des.* **138**(1), 93–104 (1992)
5. Anderson, C.E., Walker, J.D., Bless, S.J., et al.: On the velocity dependence of the L/D effect for long-rod penetrators. *Int. J. Impact Eng.* **17**(1–3), 13–24 (1995)
6. Anderson, C.E.: Analytical models for penetration mechanics: a review. *Int. J. Impact Eng.* **108**, 3–26 (2017)
7. Walker, J.D., Anderson, C.E.: A time-dependent model for long-rod penetration. *Int. J. Impact Eng.* **16**(1), 19–48 (2015)
8. Rosenberg, Z., Marmor, E., Maysel, M.: On the hydrodynamic theory of long-rod penetration. *Int. J. Impact Eng.* **10**(1), 483–486 (1990)
9. Rosenberg, Z., Dekel, E.: The relation between the penetration capability of long rods and their length to diameter ratio. *Int. J. Impact Eng.* **15**(2), 125–129 (1994)
10. Rosenberg, Z., Dekel, E.: The penetration of rigid long rods—revisited. *Int. J. Impact Eng.* **36**(4), 551–564 (2009)
11. Rosenberg, Z., Malka-Markovitz, A., Kositski, R.: Inferring the ballistic resistance of thick targets from static deep indentation tests. *Int. J. Prot. Struct.* **9**(3), 347–361 (2018)
12. Tate, A.: A theory for the deceleration of long rods after impact. *J. Mech. Phys. Solids* **15**(6), 387–399 (1967)
13. Tate, A.: Further results in the theory of long rod penetration. *J. Mech. Phys. Solids* **17**(3), 141–150 (1969)
14. Lu, Z.C., Wen, H.M.: On the penetration of high strength steel rods into semi-infinite aluminium alloy targets. *Int. J. Impact Eng.* **111**, 1–10 (2018)
15. Zhou, X.Q., Li, S.K., Liu, J.X., et al.: Self-sharpening behavior during ballistic impact of the tungsten heavy alloy rod penetrators processed by hot-hydrostatic extrusion and hot torsion. *Mater. Sci. Eng. A* **527**(18–19), 4881–4886 (2010)
16. Rong, G., Huang, D.W., Yang, M.C.: Penetrating behaviors of Zr-based metallic glass composite rods reinforced by tungsten fibers. *Theor. Appl. Fract. Mech.* **58**(1), 21–27 (2012)
17. Luo, R.M., Huang, D.W., Yang, M.C., et al.: Penetrating performance and “self-sharpening” behavior of fine-grained tungsten

- heavy alloy rod penetrators. *Mater. Sci. Eng. A* **675**, 262–270 (2016)
18. Liu, X.F., Tian, Z.L., Zhang, X.F., et al.: “Self-sharpening” tungsten high-entropy alloy. *Acta Mater.* **186**, 257–266 (2020)
 19. Magness, L.S.: High strain rate deformation behaviors of kinetic energy penetrator materials during ballistic impact. *Mech Mater.* **17**(2–3), 147–154 (1994)
 20. Conner, R.D., Dandliker, R.B., Scruggs, V., et al.: Dynamic deformation behavior of tungsten–fiber/metallic–glass matrix composites. *Int. J. Impact Eng.* **24**(5), 435–444 (2000)
 21. Choi-Yim, H., Conner, R.D., Szuecs, F., et al.: Quasi-static and dynamic deformation of tungsten reinforced Zr57Nb5Al10Cu15.4Ni12.6 bulk metallic glass matrix composites. *Scr. Mater.* **45**(9), 1039–1045 (2001)
 22. Chen, X.W., Wei, L.M., Li, J.C.: Experimental research on the long rod penetration of tungsten-fiber/Zr-based metallic glass matrix composite into Q235 steel target. *Int. J. Impact Eng.* **79**(2), 102–116 (2015)
 23. Li, J.C., Chen, X.W., Huang, F.L.: FEM analysis on the “self-sharpening” behavior of tungsten fiber/metallic glass matrix composite long rod. *Int. J. Impact Eng.* **86**(4), 67–83 (2015)
 24. Li, J.C., Chen, X.W., Huang, F.L.: FEM analysis on the deformation and failure of fiber reinforced metallic glass matrix composite. *Mater. Sci. Eng. A* **652**, 145–166 (2016)
 25. Dai, L.H., Bai, Y.L.: Basic mechanical behaviors and mechanics of shear banding in BMGs. *Int. J. Impact Eng.* **34**, 704–716 (2008)
 26. Nguyen, L.H., Ryan, S., Orifici, A.C., et al.: A penetration model for semi-infinite composite targets. *Int. J. Impact Eng.* **137**, 103438 (2020)
 27. Li, Y.Q., Gao, X.L., Fournier, A.J., et al.: Two new penetration models for ballistic clay incorporating strain-hardening, strain-rate and temperature effects. *Int. J. Mech. Sci.* **151**, 582–594 (2019)
 28. Song, W.J., Chen, X.W., Chen, P.: Effect of compressibility on the hypervelocity penetration. *Acta Mech. Sin.* **34**, 82–98 (2018)
 29. Song, W.J., Chen, X.W., Chen, P.: A simplified approximate model of compressible hypervelocity penetration. *Acta Mech. Sin.* **34**, 910–924 (2018)
 30. Li, Z., Tazan, C.C., Pradeep, K.G., et al.: A TRIP-assisted dual-phase high-entropy alloy: grain size and phase fraction effects on deformation behavior. *Acta Mater.* **131**, 323–335 (2017)
 31. Lee, M., Bless, S.: Cavity dynamics for long rod penetration (No. IAT. R-0094). Texas University at Austin Institute for Advanced Technology (1996)
 32. Nino, Y., Marcelo, H.G.: Experiments on particle–turbulence interactions in the near-wall region of an open channel flow: implications for sediment transport. *J. Fluid Mech.* **326**(1), 285–319 (1996)
 33. Labusch, R.: A statistical theory of solid solution hardening. *Phys. Status Solidi B.* **41**(2), 659–669 (1970)
 34. Labusch, R.: Statistische theorien der mischkristallhärtung. *Acta Metall.* **20**(7), 917–927 (1972)
 35. Senkov, O.N., Scott, J.M., Senkova, S.V., et al.: Microstructure and room temperature properties of a high-entropy TaNbHfZrTi alloy. *J. Alloys Compd.* **509**(20), 6043–6048 (2011)
 36. Yao, H., Qiao, J.W., Gao, M.C., et al.: MoNbTaV medium-entropy alloy. *Entropy* **18**(5), 189 (2016)
 37. Chen, H.H., Zhang, X.F., Liu, C., et al.: Analysis of material flow around projectile nose by elbow-streamline model during long-rod projectile penetrating into steel target. *Acta Armamentarii.* **40**(9), 1787–1796 (2019) [in Chinese]
 38. Lundberg, P., Renström, R., Lundberg, B.: Impact of metallic projectiles on ceramic targets: transition between interface defeat and penetration. *Int. J. Impact Eng.* **24**(3), 259–275 (2000)
 39. Lundberg, P., Renström, R., Lundberg, B.: Impact of conical tungsten projectiles on flat silicon carbide targets: transition from interface defeat to penetration. *Int. J. Impact Eng.* **32**(11), 1842–1856 (2006)
 40. Jiao, W.J., Chen, X.W.: Influence of the mushroomed projectile’s head geometry on long-rod penetration. *Int. J. Impact Eng.* **148**, 103769 (2021)
 41. Jiao, W.J., Chen, X.W.: Approximate solutions of the Alekseevskii–Tate model of long-rod penetration. *Acta Mech. Sin.* **34**, 334–348 (2018)
 42. Jiao, W.J., Chen, X.W.: Analysis of the velocity relationship and deceleration of long-rod penetration. *Acta Mech. Sin.* **35**, 773–785 (2019)

Publisher’s Note Springer Nature remains neutral with regard to jurisdictional claims in published maps and institutional affiliations.